Nanoscale Horizons

ROYAL SOCIETY OF CHEMISTRY

COMMUNICATION

View Article Online
View Journal | View Issue

Cite this: *Nanoscale Horiz.*, 2024, 9, 1341

Received 29th December 2023,
Accepted 18th April 2024

DOI: 10.1039/d3nh00594a

rsc.li/nanoscale-horizons

Intermetallics with sp–d orbital hybridisation: morphologies, stabilities and work functions of In–Pd particles at the nanoscale†

Alexis Front,*[abc] Clovis Lapointe[ad] and Émilie Gaudry *[a]

The field of intermetallic catalysts, alloying a p-block and a transition metal to form a pM–TM bimetallic alloy, is experiencing robust growth, emerging as a vibrant frontier in catalysis research. Although such materials are increasingly used in the form of nanoparticles, a precise description of their atomic arrangements at the nanoscale remains scarce. Based on the In–Pd binary as a typical pM–TM system, we performed density functional theory calculations to investigate the morphologies, relative stabilities and electronic properties of 24 Å and 36 Å nanoparticles built from the In_3Pd_2, InPd and $InPd_3$ compounds. Wulff equilibrium structures are compared to other ordered and disordered structures. Surface energies are computed to discuss their thermodynamic stability, while work functions are calculated to examine their electronic structures. For any compound, increasing the size leads to the stabilisation of Wulff polyhedra, which are found to offer smaller surface energies than non-crystalline and chemically disordered structures. Disordered In_3Pd_2 and InPd nanoparticles show a tendency towards amorphisation, owing to repulsive short In–In bonds. Tuning nanoparticles' work functions can be achieved through the control of the surface structure and composition, by virtue of the roughly linear correlation found between the surface composition and the work function which nevertheless includes a certain number of outliers. This work paves the way to rationalisation of both structural and electronic properties of pM–TM nanoparticles.

New concepts

Intermetallic nanoparticles, combining p-block and transition metals to form pM–TM binary alloys, are of paramount importance across a broad spectrum of applications, underscoring the crucial significance of studying their nanoscale structures. Through the In–Pd system, novel insights have been uncovered, shedding new light on the structure–property relationships within this type of pM–TM intermetallic nanoparticles. Based on density functional theory calculations, regarding structures of In_3Pd_2, InPd and $InPd_3$ nanoparticles, within sizes ranging from 25 Å to 34 Å, we show that non-crystalline morphologies are not likely. Wulff-type morphologies are found thermodynamically more stable in these ordered systems, the larger the size, the better. Moreover, our computations reveal that disordered In-rich nanoparticles tend to undergo amorphisation, driven by destabilising In–In interactions, while the crystalline character of nanoparticles with a large Pd content is kept. Concerning nanoparticle properties, using an original computational method, we bring to light a roughly linear correlation between the surface composition and the work function, although it nonetheless incorporates a certain number of outliers. Amorphous particles have a lower work function compared to crystalline particles, attributable to their surface composition enriched in indium. This study establishes a foundation for systematically understanding the structural and electronic characteristics of pM–TM nanoparticles.

1. Introduction

The development of technologically relevant nanoparticles (NPs) has seen unprecedented growth in recent years. Initially used by artisans, mainly for their optical properties, albeit without the knowledge of their nature,[1–3] they are nowadays used to develop many different applications, in biomedicine,[4–6] energy,[7–9] and information technologies,[10,11] with the most widespread applications likely being in catalysis. In the latter case, mono-metallic precious and transition metal NPs have played a major role,[12–15] demonstrated, among others, by the relevance of gold NPs in CO oxidation,[16] of copper-based NPs in methanol production from syngas ($CO + H_2$),[17] of silver NPs in solar-driven photocatalytic water splitting, CO_2 reduction and degradation of organic pollutants,[18] and also of platinum,

[a] Université de Lorraine, CNRS, Institut Jean Lamour, UMR 7198, Campus Artem, 2 allée André Guinier, F-54011, Nancy, France. E-mail: alexis.front@aalto.fi, emilie.gaudry@univ-lorraine.fr
[b] Department of Chemistry and Materials Science, Aalto University, 02150 Espoo, Finland
[c] Department of Applied physics, Aalto university, P.O. Box 11000, FI-00076 Aalto, Finland
[d] Université Paris-Saclay, CEA, Service de Recherche en Corrosion et Comportement des Matériaux, SRMP, 91191 Gif-sur-Yvette, France

† Electronic supplementary information (ESI) available. See DOI: https://doi.org/10.1039/d3nh00594a

iridium and ruthenium based NPs in the hydrogen evolution reaction (HER), oxygen reduction reaction (ORR) and oxygen evolution reaction (OER).[19] This is attributed to the ability of metals to activate chemical bonds through d-electrons or d-empty orbitals,[20] and also to the quantitative understanding that has been established in transition-metal catalysis over recent years.[21,22]

Elemental transition metals however struggle to satisfy the numerous and sometimes contradictory needs of high-performance catalysts, *i.e.* high activity, tractable selectivity, low cost and good stability. Tailoring atomic arrangements and chemical compositions are key approaches to circumvent previous limitations, generally achieved by alloying, faceting, and nanostructuring, as well as selecting crystal structures and surface orientations.[23–25] Thus, many bimetallic NPs have been developed over the last few years, generally by associating two precious metals or a noble metal and a first-row transition metal. The so-called "synergistic" effects between the two metals are known to greatly enhance the catalyst efficiency in many cases. Hence, Pd–Au alloys are likely among the most widely used solid-solution alloys in all fields of catalysis (ref. 25 and references therein), while Pt-based nanoalloys, especially, in the Pt–Ni system, are considered to be one of the most promising catalysts for the oxygen reduction reaction (ORR) – bottleneck restricting the large-scale commercialisation of fuel cell vehicles[26] – able to improve by a factor of 4 to 10 the catalytic performance of the ORR in comparison to commercial Pt/C.[27,28]

The specific performances of bimetallic catalysts are typically attributed to electronic and geometric effects, including orbital hybridisation and active site isolation. Up to now, most theoretical investigations have relied on infinite slabs, while experimental catalysts are generally synthesised in the form of nanoparticles. At the nanoscale, mixing two late transition metals leads to a large variety of configurations, including core–shell, segregated, multishell, ordered or solid-solution alloys.[29] The atomic arrangements can greatly differ from the ones resulting from bulk truncation, especially, when the composition range of a given phase is large and its formation enthalpy is low. It is for instance the case of Pt–Ni nanoalloys ($|\Delta H_f| < 0.1$ eV per at.),[30] for which icosahedral core–shell and multishell morphologies have been predicted to be likely for 147–923 atom NPs.[31]

Compared to conventional d–d bimetallic NPs, the knowledge of systems combining transition and p-block metals – *e.g.* Al, Zn, Ga, Cd, In and Sn within the first periods of the periodic table – is little and is currently quickly developing. Among them, In–Pd phases have been identified as relevant catalysts for several reactions. This is especially the case (i) for methanol steam reforming, for which In_xPd_y/In_2O_3 aerogels exhibit excellent CO_2 selectivities (99%),[32] (ii) for methanol synthesis, for which In–Pd NPs show higher CH_3 OH rates (70%) and selectivities (80% at 270 °C) compared to conventional $Cu/ZnO/Al_2O_3$,[33,34] and (iii) for hydrogenation/dehydrogenation reactions, for which the addition of In to Pd improves the catalytic performances, likely attributed to site isolation.[35–39] The formation of In–Pd intermetallics can also reduce the catalyst coking[37,38] and poisoning.[40] Such performances strongly depend on the catalyst's chemical composition and surface structure. Indeed, recent studies highlight the better catalytic performances in acetylene hydrogenation of bimetallic In–Pd at an In : Pd ratio of 0.8,[37] and a higher selectivity (92% *vs.* 21% at 90 °C)[41] of 1 : 1 InPd NPs than that of $InPd_3$ NPs, attributed to the different types of mainly exposed facets – (110) and (111) for 1 : 1 InPd and $InPd_3$, respectively. Thus, the controlled synthesis of pM–TM (p-block metal–transition metal) NPs is crucial to design catalysts with optimal performances.

The rich structural chemistry of pM–TM systems, typically attributed to the large formation enthalpy of 1 : 1 bulk compounds ($|\Delta H_f| > 0.1$ eV per at. in many cases),[30,42] yields too many intermetallics in the bulk phase diagram,[43] and thus is expected to lead to a substantial variety of atomic arrangements at the nanoscale. Within the In–Pd system, the large compositional range of the 1 : 1 InPd phase, extending from 45 at%Pd to 61.5 at%Pd, *i.e.* much larger than other that of In–Pd binaries,[44] likely eases the experimental synthesis of InPd NPs, with sizes down to 10 nm. Other single-phase NPs have however recently been synthesised, like $InPd_3$ (size 5 nm),[39] In_3Pd_2 (size 90 nm),[45] and In_7Pd_3 (sizes in the range of 60–90 nm).[39,45] Moreover, for particle sizes below 3 nm, core–shell structures have been identified, with a Pd core and a 1 : 1 InPd shell, when the In : Pd atomic ratio is 0.8.[35] Ordered 1 : 1 InPd particles, with an unalloyed In shell, have also been formed, with a rather high In : Pd ratio (value = 2).[35] However, no disordered crystalline structure has ever been observed, nor any non-crystalline structures, in contrast to the literature on d–d nanocrystals.[46–48]

Overall, the development of a synthetic approach for ordered intermetallic nanocrystals is challenging.[49] Thus, numerical methods are crucial to understand, explain and predict nanoalloys' morphologies, structures and properties.[50,51] Current computational resources combined with density functional theory (DFT) are now able to calculate key quantities, like the nanoparticles' surface energy, one of the most important quantities to discuss their thermodynamic stability,[31,52,53] which can be compared to experimental measurements.[54] Because chemisorption typically involves the Fermi level of the catalysts and the HOMOs/LUMOs (highest occupied/lowest unoccupied molecular orbitals) of the reactants, the work function is one important feature for catalysis.[55–57] In this work, by focusing on NPs with the 1 : 1 InPd composition, as well as on one composition in the Pd-rich side ($InPd_3$) and on one composition in the In-rich side (In_3Pd_2), we show that ordered structures are stable, at least when compared to non-crystalline structures. We also highlight the amorphisation of disordered structures, driven by destabilising In–In interactions. Finally, trends between the NPs' work functions and their morphologies, sizes and chemical compositions are examined, thus opening a way to design NPs with specific properties.

2 Results and discussion

2.1 The In–Pd system

The bulk In–Pd system presents a rich phase diagram, with six intermetallic compounds at room temperature[44]: In_7Pd_3

Table 1 Space groups, cell parameters and formation enthalpies of the In–Pd compounds considered in this study

Compound	Space group	a (Å)	c (Å)	ΔH_f (eV per at.)	
In_3Pd_2	$P\bar{3}m1$	4.642	5.586	−0.476	PBE (our work)
		4.642	5.586	−0.464	PBE[30]
		4.535	5.512	−0.59	Exp.[59,63]
InPd	$Pm\bar{3}m$	3.31		−0.489	PBE (our work)
		3.31		−0.497	PBE[30]
		3.250		−0.72	Exp.[59,63]
$InPd_3$	$Pm\bar{3}m$	4.045		−0.4396	PBE (our work)
		4.045		−0.438	PBE[30]
		4.027		−0.554	Exp.[58,64]

($Im\bar{3}m$ space group, $cI40$), In_3Pd_2 ($P\bar{3}m1$ space group, $hP5$), α-$InPd_3$ ($I4/mmm$ space group, $tI8$), α-$InPd_2$ ($Pnma$ space group, $oP12$), In_3Pd_5 ($Pbam$ space group, $oP16$), and InPd ($Pm\bar{3}m$ space group, $cP2$). Beside the 1 : 1 InPd compound, we have considered in this work one In-rich compound (In_3Pd_2) and one Pd-rich compound ($InPd_3$). Depending on the experimental conditions, the $InPd_3$ compound can be synthesised with several crystal structures, including $AuCu_3$-type (cubic, $Pm\bar{3}m$ space group, cP4),[58] $ZrAl_3$-type (tetragonal, $I4/mmm$ space group, tl16),[58] and $CuInPt_2$-type (tetragonal, $I4/mmm$ space group, tP4).[59] In this work, we focus on three In–Pd compounds (Table 1): cubic InPd of CsCl-type and cubic $InPd_3$ of $AuCu_3$-type, in connection with the extensive investigations of nanoalloys with cubic structures.[60–62] We also consider the In_3Pd_2 phase that crystallises in the trigonal system, for which investigations at the nanoscale are nonexistent, as far as we know.

The calculated electronic density of states of the three compounds is represented in Fig. 1. The low energy range (−10 eV to −5 eV) is mainly formed by In-states, with a contribution of Pd-states. As previously mentioned in ref. 65 and 66 on $GaPd_2$ and In_3Pd_5, this region reflects the chemical binding in the compounds. The remaining part shows one strong contribution from Pd d-states, in a form of a band, located above 4 eV, whose bandwidth increases with the Pd content. Indeed, the isolation of Pd sites in In_3Pd_2 and InPd, more pronounced as the In concentration increases, results in a narrow d-band, the hybridisation between Pd-d states being weak. In contrast, the d–d hybridisation in $InPd_3$ leads to a large d-band (roughly two times as large as in In_3Pd_2 and InPd). Such differences in the electronic structure may be at the origin of the distinct behaviour of In_3Pd_2 and InPd NPs, in comparison to $InPd_3$ NPs.

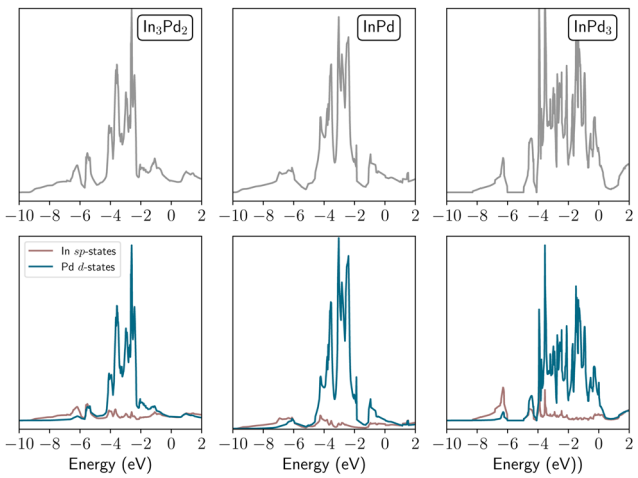

Fig. 1 Density of states (DOS) of In_3Pd_2 (left), InPd (middle) and $InPd_3$ (right) bulk compounds. The total DOS of each bulk compound is given (in grey), along with the In-sp and Pd-d contributions (in brown and blue, respectively).

2.2 Surface energies and morphologies of NPs based on the Wulff construction

Overall, the equilibrium shape of free nanoparticles is known to be given by the Wulff construction, assuming the bulk crystal structure, and based on the ratios between the compound's surface energies.[67] Energies of several low-index surfaces have been computed as a function of the Pd's chemical potential (Tables S1 and S2, ESI†) and are shown in Fig. 2. The three subfigures correspond to energies of In_3Pd_2 (left), InPd (middle) and $InPd_3$ (right) low-index surfaces. A few additional orientations have been considered, but are not presented in Fig. 2 (In_3Pd_2 ($2\bar{1}0$), InPd (102) and $InPd_3$ (112)). In the following, we define the In- and the Pd-rich limit by the situations with $\Delta\mu_{Pd} = 0$ eV and $\Delta\mu_{In} = 0$ eV, respectively. This is valid for the three compositions. Nevertheless, it should be mentioned that the value of $\Delta\mu_{Pd}$ at the In-rich limit ($\Delta\mu_{In} = 0$ eV) depends on the considered compound. It is $\Delta\mu_{Pd} = -0.978$ eV, $\Delta\mu_{Pd} = -0.586$ eV and $\Delta\mu_{Pd} = -1.190$ eV in the case of InPd, $InPd_3$ and In_3Pd_2, respectively.

On the whole, pure Pd-terminated surfaces are calculated to present a rather high surface energy, (label 12 for InPd in Fig. 2, not represented for $InPd_3$), while stable surfaces are found among mixed terminations. It is the case for $InPd_3$ (100) (label 15 in Fig. 2), with a particularly low surface energy at the In-rich limit ($\gamma = 0.491$ J m^{-2}) that increases at the Pd-rich limit ($\gamma = 1.072$ J m^{-2}). The latter value is similar to the one found for $InPd_3$ (111) (1.046 J m^{-2}) for $\Delta\mu_{Pd} = 0$. Indeed, both $InPd_3$ (111) and $InPd_3$ (100) terminations contain In and Pd atoms. The $InPd_3$ (111) topmost plane is stoichiometric and shows a higher atomic density than the mixed termination of $InPd_3$ (100) – 0.15 at per Å^2 *vs.* 0.12 at per Å^2. But the In content of the mixed $InPd_3$ (100) termination is larger (0.06 In at. per Å^2, *vs.* 0.04 In at. per Å^2 for the stoichiometric surface), thus leading to a stabilising effect. Indeed, the presence of In atoms on the surface is less unfavourable than that of Pd. Similar surface energies are also calculated for InPd(100), InPd(110) and InPd(111) at the In-rich limit, and for InPd(111) and InPd(110) at the Pd-rich limit. The situation is rather complex for In_3Pd_2, with relative stabilities calculated to rank as $\gamma_{(101)} < \gamma_{(100)} < \gamma_{(110)} < \gamma_{(001)}$ in the In-rich and $\gamma_{(001)} < \gamma_{(100)} < \gamma_{(110)} < \gamma_{(101)}$ in the Pd-rich side.

Based on the surface energies at the In- and Pd-rich limits, and using the Wulff approach, two types of NPs are built (Fig. 3). Their morphologies strongly depend on the chemical potentials. The $InPd_3$ NP exhibits a cubic shape in the In-rich side and a truncated octahedral (TOh) morphology – typically

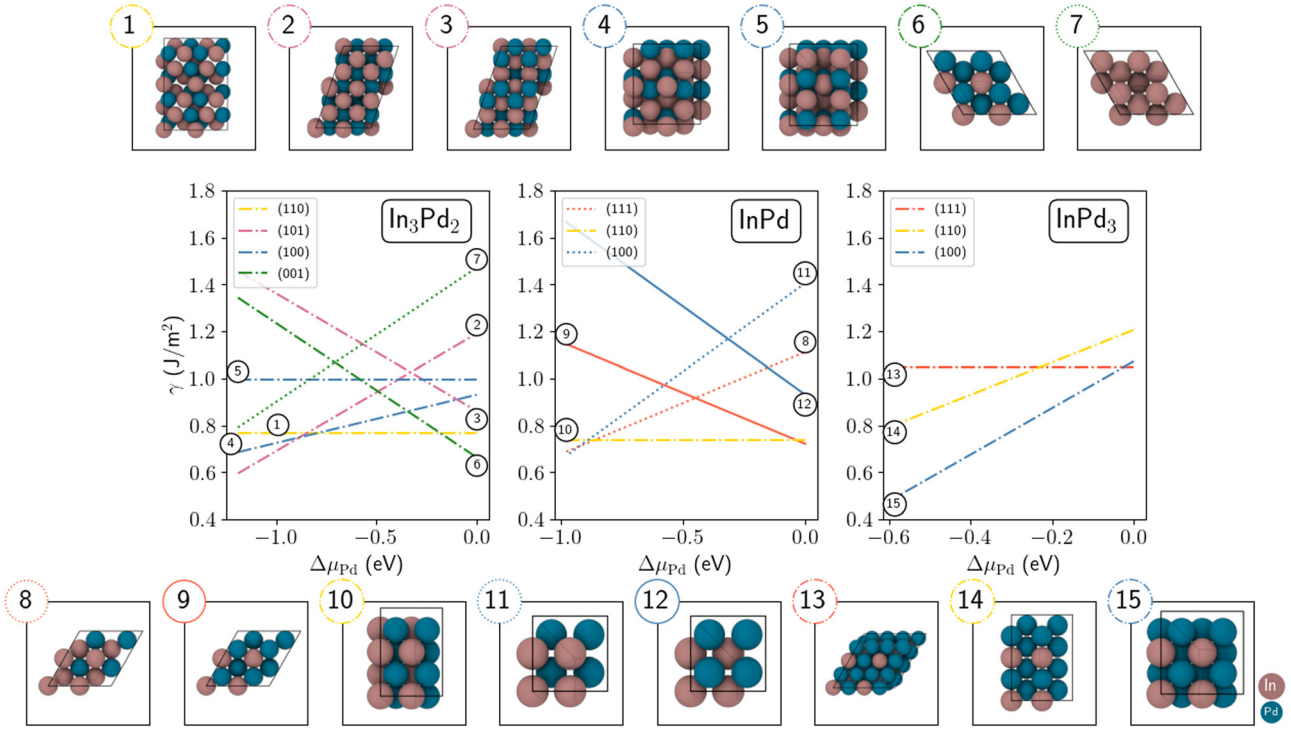

Fig. 2 Surface energies of In_3Pd_2 (*hkl*) (left), InPd (*hkl*) (middle) and $InPd_3$ (*hkl*) (right) as a function of $\Delta\mu_{Pd} = \mu_{Pd} - \mu_{Pd}^{b}$, where μ_{Pd} is the chemical potential of Pd in the compound and μ_{Pd}^{b} is the cohesive energy of elemental Pd bulk. Pure Pd, pure In and mixed terminations are shown with solid, dashed and dash-dotted lines, respectively. Only the most stable surfaces are represented. Colour code for surface terminations: Pd = blue and In = brown.

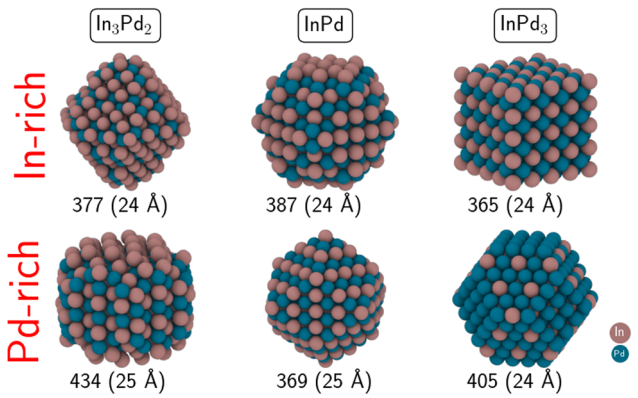

Fig. 3 Morphologies of In_3Pd_2 (left), InPd (middle) and $InPd_3$ (right) NPs based on the Wulff construction. The diameter of each NP is given, along with its number of atoms. The top row corresponds to the NP morphology at the In-rich side whereas the bottom row corresponds to the Pd-rich side. Colour code: Pd = blue and In = brown.

the Wulff polyhedra of TM alloys – in the Pd-rich side. Because the stoichiometric InPd(110) surface presents a low energy, independent of the chemical potentials, the InPd NP morphology is similar at both In- and Pd-rich limits, characterised by large (110) facets. The main difference between the two cases lies in small (100) facets observed at the In-rich side, due to the low InPd(100) surface energy at $\Delta\mu_{In} = 0$. The In_3Pd_2 NP displays a cylindrical shape at the Pd-rich limit, mainly due to the stability of the $In_3Pd_2(001)$ surface for $\Delta\mu_{Pd} = 0$. In the In-rich side, the stability of the $In_3Pd_2(110)$ surface leads to a shape with steeper facets. In the following, Wulff polyhedra, built using most stable facets at the In-rich and Pd-rich limits (Fig. 2 and Table S2, Section S2, ESI†), are labelled WP_{In} and WP_{Pd}, respectively.

2.3 Stability of bimetallic In–Pd nanoparticles

The calculation of surface energies requires an infinite reservoir of particles, which becomes questionable when the size of the NPs is not large enough. Therefore, we build two types of NPs: on the one hand, NPs with a diameter between 22 Å and 28 Å (300 to 500 atoms, called "small" NPs in the following), and on the other hand, NPs with a diameter larger than 36 Å (made of around 1000 to 1200 atoms, called "large" NPs in the following).

Moreover, we also consider in this work other geometries, that can offer dense fcc{111} and fcc{100} facets when dealing with fcc metals, but whose relevance to the case of non-fcc In–Pd NPs mostly relies on their spherical shape. We focused on icosahedron (Ih), decahedron (Dh), octahedron (Oh) and cuboctahedron (Cubo) shapes (Fig. 4). These morphologies have been chosen because, for metal NPs, (i) non-crystalline Ih and Dh geometries are typically the ones of small to intermediate sized NPs,[68,69] while crystalline Oh and Cubo geometries are commonly in competition with the Wulff polyhedron for large size NPs. Below, not to be confused with the

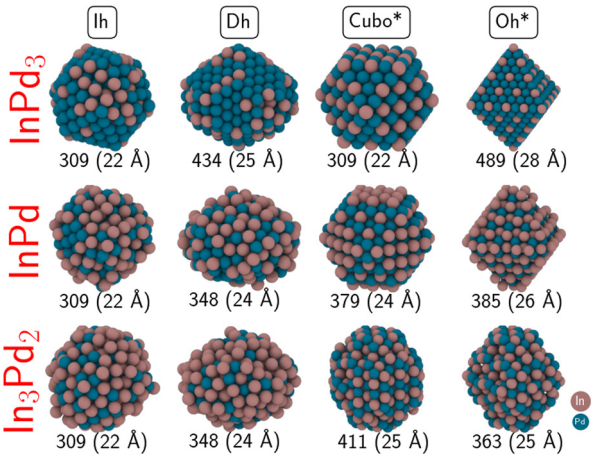

Fig. 4 Non-crystalline (Ih and Dh) and crystalline (Oh* and Cubo*) morphologies of In_3Pd_2, InPd and $InPd_3$ NPs. The diameter of each NP is given, along with its number of atoms. Colour code: Pd = blue and In = brown.

conventional Cubo and Oh shapes of $L1_2$ bimetallic NPs (as is $InPd_3$), we rename Oh by Oh* and Cubo by Cubo*, to indicate that * corresponds to In_3Pd_2 or InPd. Both ordered and chemically disordered NPs are generated. Eleven structures have been relaxed. Total energies of chemically disordered WPs result from an average of over nine or ten configurations, generated by random shuffling of atoms in the structure. While energy differences between the different configurations can be rather high – it reaches more than 60 meV per at. for Wulff shaped In_3Pd_2 NPs, the dispersion of energies after structural relaxation is less than a few meV per at. (20 meV per at. for Wulff shaped In_3Pd_2 NPs). The NP stabilities have been evaluated through their surface energies, calculated as a function of the Pd's chemical potential. They are shown in Fig. 5. The three sub-figures correspond to NPs built from In_3Pd_2 (left), InPd (middle) and $InPd_3$ (right).

In the following, we first discuss the case of small NPs (Fig. 5). At the Pd-rich limit ($\Delta\mu_{Pd} = 0$), the most stable configuration of $InPd_3$ NP is WP_{In}, which exhibits only low energy mixed (100) facets, *i.e.* faces composed of both In and Pd. At lower $\Delta\mu_{Pd}$, this structure is progressively destabilised and the WP_{Pd} configuration, characterised by (100) and (111) facets, becomes the most stable one in the region -0.59 eV $< \Delta\mu_{Pd} < -0.21$ eV. Interestingly, at the crossover between WP_{In} and WP_{Pd} (*i.e.* -0.21 eV $< \Delta\mu_{Pd} < -0.19$ eV), the most stable configuration is the Oh structure with only mixed (111) facets. Increasing the indium concentration to InPd leads to a situation, where WP_{Pd}, characterised by only mixed (110) facets, thus forming a quasi-spherical NP, is the most stable configuration on almost the whole range of Pd's chemical potentials. At the Pd-rich limit, there is a competition between WP_{Pd} and WP_{In}, which mainly exhibits (100) facets. At the In-rich limit, Oh* is the most stable morphology. Focusing on In_3Pd_2 NPs, the most stable configurations are WP_{In} at the Pd-rich side, and Cubo* and Oh* at the In-rich side. The surface energies of Cubo* and Oh* are close to each other, Cubo* becoming more favourable than Oh* at the In-rich side. Overall non-crystalline and disordered structures are not favoured on the whole range of $\Delta\mu_{Pd}$, a consequence of the large formation enthalpy of the In–Pd compounds ($|\Delta H_f|$), which acts as a driving force to stabilise chemical order and crystalline structures (see Section 2.4). This is rather different from the observations on transition metal nanoalloys ($|\Delta H_f| < 0.1$eV per at. in many cases), in which many morphologies distinct from polyhedral shapes might occur.[70–73]

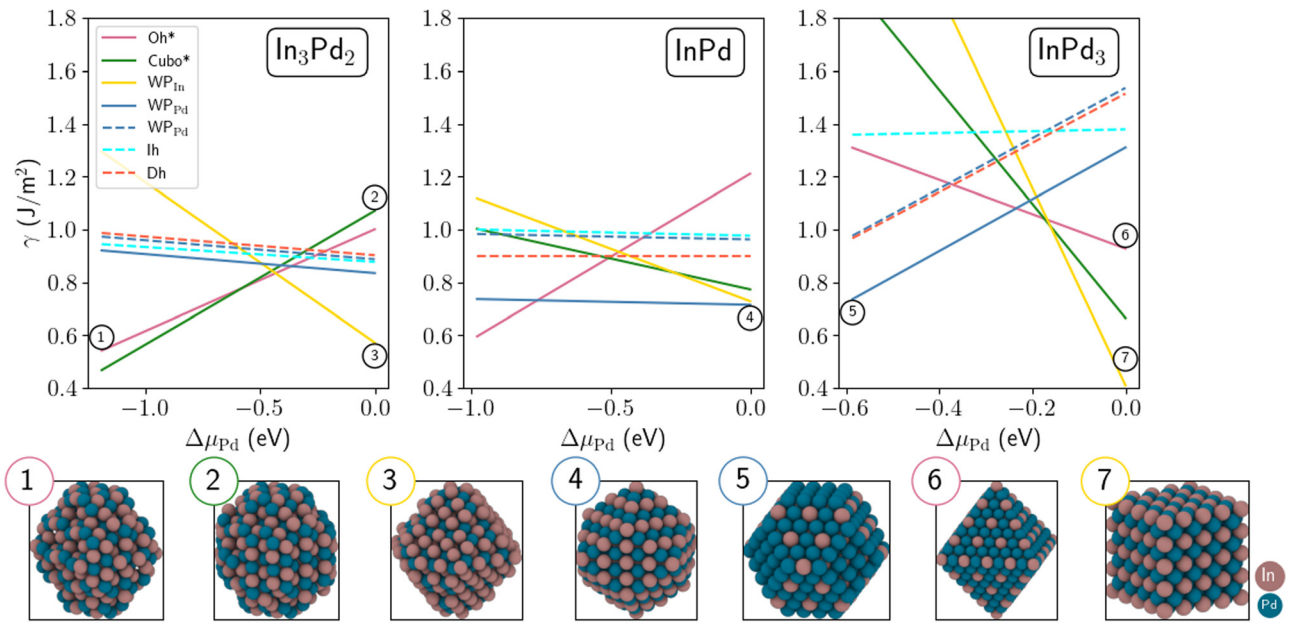

Fig. 5 Surface energies of In_3Pd_2 (left), InPd (middle) and $InPd_3$ (right) NPs as a function of $\Delta\mu_{Pd} = \mu_{Pd} - \mu_{Pd}^{b}$. Chemically ordered and disordered NPs are shown with full and dashed lines, respectively. Colour code: Pd = blue and In = brown.

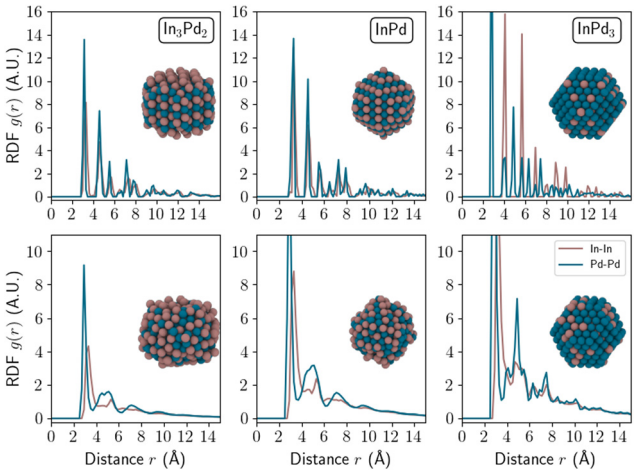

Fig. 6 Radial distribution function of In–In (brown) and Pd–Pd (blue) bonds as a function of the distance from the NP centre (r). The considered NPs are small WP_{Pd} nanoparticles (diameter 24 Å) of In_3Pd_2 (left), InPd (middle), and $InPd_3$ (right) compounds. The top and bottom rows correspond to ordered and disordered WP_{Pd} NPs, respectively. Colour code: Pd = blue and In = brown.

To deepen our analysis, we computed the radial distribution function (RDF) along the radius of the NP as displayed in Fig. 6. In the ordered state, NP RDFs are characterised by alternating sharp peaks, for any considered In–Pd compound, *i.e.* In_3Pd_2, InPd and $InPd_3$. The computed first neighbour distances for In–Pd (2.78 Å) in InPd NPs are found to be in excellent agreement with experimental data: according to X-ray diffraction and X-ray absorption spectroscopy, the values are 2.81 Å and 2.79 Å, respectively, for small InPd NPs (27 Å, label Pd–In 2.0 in ref. 35). In addition, our computed value for the first neighbour Pd–Pd distance (3.22 Å) is also in good agreement with the same distance in bulk InPd (3.25 Å).

In the case of disordered $InPd_3$, the RDF exhibits wider peaks than in the ordered state. For disordered compounds with larger In concentrations, *i.e.* for disordered InPd and In_3Pd_2, only one sharp peak is still present, corresponding to the closest neighbours. It suggests an amorphisation of the nanoparticles. This is in agreement with recent observations of amorphous disordered NP structures in the pM–TM system.[74] This is however quite different from the observations on transition metal nanoalloys with crystalline disordered structures, which do not present any amorphisation.[75]

The size of NPs is known to have a strong impact on their stability. Indeed, increasing the size might change the NP terminations and thus their Pd contents, leading to a drastic modification of their surface energies. Size effects are investigated here by comparing small (300–500 atoms) and large NPs ($\simeq$1000 to 1200 atoms, Fig. 7). In the case of $InPd_3$, in the Pd-rich side, the most stable configuration is WP_{In} (thick yellow line, Fig. 7), *i.e.* the same configuration as that identified for small sizes. As μ_{Pd} decreases, this structure is progressively destabilised in favour of the Cubo morphology (thick green line, Fig. 7). The latter morphology is then the most stable one, in the range -0.59 eV $< \Delta\mu_{Pd} < -0.21$ eV. This is consistent with the result found for smaller NPs, for which the WP_{Pd} structure has been found to be the most stable one (thin yellow line, Fig. 5). Indeed, both Cubo and WP_{Pd} exhibit (100) and (111) facets, the core being the same in both cases. The only difference between Cubo and WP_{Pd} NP is their facet sizes. In the case of InPd, the most stable morphology is WP_{Pd} for both small and large NPs (thick and thin blue lines, Fig. 7), the surface energy decreases by around 0.05 J m^{-2} when the

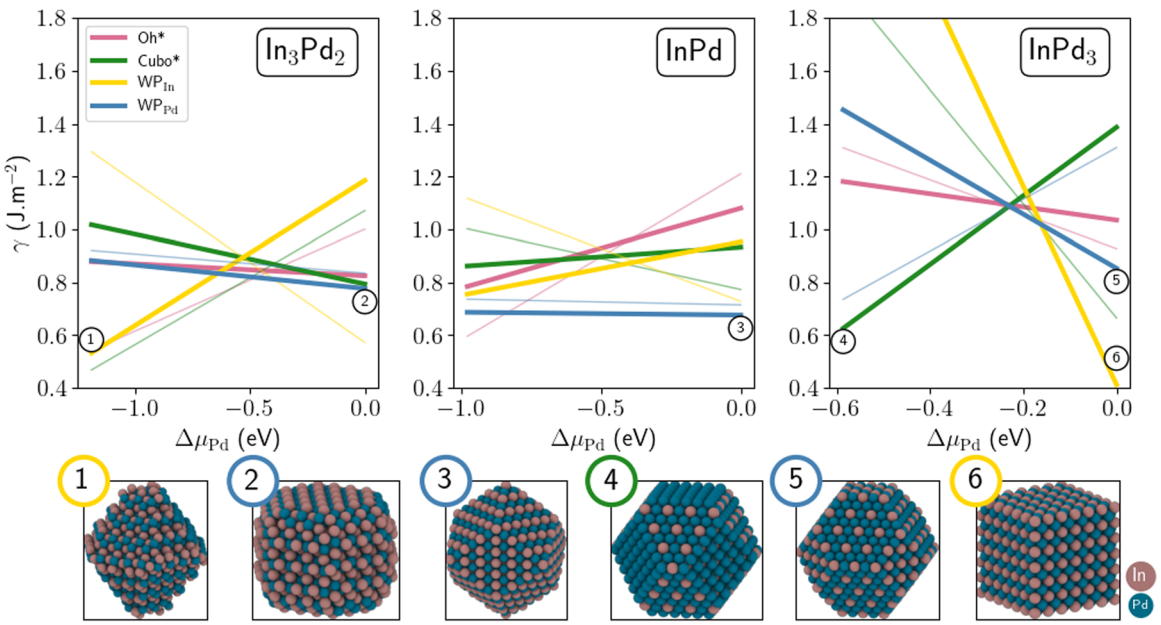

Fig. 7 Surface energies of In_3Pd_2 (left), InPd (middle) and $InPd_3$ (right) NPs as a function of $\Delta\mu_{Pd}$. Thin and thick lines represent small and large NPs, respectively. Colour code: Pd = blue and In = brown.

number of atoms in the NP is multiplied by three, approximately. In the case of In_3Pd_2, the Wulff polyhedra is the most stable structure for large NPs, *i.e.* WP_{Pd} at $\Delta\mu_{Pd} = 0$ (thick blue line, Fig. 7) and WP_{In} at $\Delta\mu_{Pd} = -1.19$ eV with a crossover around $\Delta\mu_{Pd} = -0.6$ eV. This is a direct signature of the size effect. The Oh* and Cubo* morphologies that are typical for fcc metals are not favoured in $InPd_3$ NPs, at least when $\Delta\mu_{Pd} = 0$, even if bulk $InPd_3$ presents some similarities with fcc metals.

2.4. In–In short range interactions drive possible amorphisations of NPs

We now quantitatively investigate the amorphisation induced by chemical disorder in small In–Pd NPs. Our discussion is based on the pseudo-pairwise electrostatic interaction ($\tilde{V}_{ij}(r)$) defined as:

$$\tilde{V}_{ij}(r) = \frac{\Delta q_i \Delta q_j}{4\pi\varepsilon_0}\langle\chi_i|\hat{r}_{ij}^{-1}|\chi_j\rangle, \quad (1)$$

where Δq_i is the effective charge of atom i, ε_0 is the vacuum permittivity, $\hat{r}_{ij}$ is the distance operator between atom i and atom j and $|\chi_i\rangle$ values are *ad-hoc* localised electronic wave function basis vectors for electrons of atom i. The effective electrostatic potential ($\tilde{V}_{ij}(r)$) for a given pair of atoms (ij) separated by a distance r is positive and negative when the ij interaction is repulsive and attractive, respectively. To estimate $\langle\chi_i|\hat{r}_{ij}^{-1}|\chi_j\rangle$, we have performed a crystal orbital overlap population (COOP) analysis[76] using the Lobster package[77] which is coupled to the VASP software.[78–80] All bonds with lengths below 5.5 Å have been considered. Then, we have computed the following quantity:

$$\langle\tilde{V}_{ij}\rangle(r_b, \delta r) = \frac{1}{\int_0^\infty 1_{|r_b - r| \le \delta r} dr}\int_0^\infty \tilde{V}_{ij}(r) 1_{|r_b - r| \le \delta r} dr \quad (2)$$

where $1_{|r_b - r| \le \delta r}$ is the indicator function, which is equal to 1 if $|r_b - r| \le \delta r$ and 0 otherwise (δr is set to 0.55 Å). The radial $\langle\tilde{V}_{ij}\rangle$ quantity defined in eqn (2) is an average of the $\tilde{V}_{ij}(r)$ electrostatic bond energies for ij atom pairs in the bond distance range of $[r_b - \delta r, r_b + \delta r]$.

In Fig. 8 and in Table S3 (ESI†), we systematically compare, for a given composition, averaged $\tilde{V}_{ij}$ energies for chemically ordered and chemically disordered nanoparticles. The top row displays ordered WP_{Pd} whereas the bottom row represents disordered WP_{Pd}. Dots are brute data, their sizes are proportional to the number of bonds at a bond length equal to r_b and dashed lines are fitted Pauling functions.[81] For all compositions (In_3Pd_2, InPd, and $InPd_3$), the magnitudes of electrostatic pair energies for In–In bonds are much larger than the ones of In–Pd and Pd–Pd. Therefore, we focus in the following on In–In bonds to investigate the stability. In $InPd_3$ WP_{Pd} NPs, most In–In bonds are attractive, suggesting that In–In interactions tend to stabilise NPs. In InPd and In_3Pd_2 WP_{Pd} NPs, the In–In electrostatic pair energy is a monotonically decreasing function, with a high positive maximum close to $r_c = 3.0$ Å (Fig. 8). Since positive values indicate repulsive interactions, the short In–In bonds in InPd and $InPd_2$ WP_{Pd} NPs are destabilising.

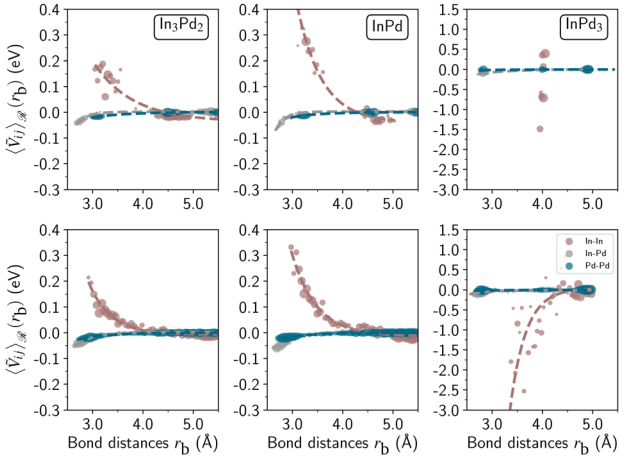

Fig. 8 Radial average $\tilde{V}_{ij}$ energy ($\langle\tilde{V}_{ij}\rangle$ (r_b)) of In–In bonds (brown), Pd–Pd bonds (blue) and In–Pd bonds (grey) for small NPs (diameter 24 Å) built by the Wulff construction using In_3Pd_2 (left), InPd (middle), $InPd_3$ (right) bulk compounds. The top and bottom rows display ordered and disordered WP_{Pd}, respectively. Dots are brute data and dashed lines result from interpolation. Dot sizes are proportional to bond numbers.

To avoid such non-favourable interactions, the structure is modified and as a consequence it induces amorphisation in the corresponding NP structures. It is also evidenced by Table S3 (ESI†), where differences appear between panel A (non-relaxed structures) and panel B (relaxed structures for InPd and In_3Pd_2 WP_{Pd} NPs (bottom line, left and middle columns), with a minimum appearing for r close to 3 Å.

Looking more precisely at the region, called $\mathscr{S}$, localised between 3 Å and 4 Å, relevant for the shortest In–In bonds and then meaningful for the stability, we found that $\mathscr{S}$ is an attractive (respectively, repulsive) domain for In–In bonds in $InPd_3$ NPs (respectively, in InPd and In_3Pd_2 NPs). Based on the analysis performed in Section 2.3 (Fig. 6), we have recalculated the radial distribution functions, focusing on the $\mathscr{S}$ domain (Fig. 9). We have plotted RDFs before and after the structural optimisation, *i.e.* we considered both non-relaxed (Fig. 9A) and relaxed (Fig. 9B) NPs. In each panel (A and B), the top and bottom rows display ordered and disordered WP_{Pd} NPs, respectively. In each sub-figure, the $\mathscr{S}$ domain is highlighted in colour. The blue filled area represents the attractive In–In interactions in $InPd_3$ NPs, while the red filled areas represent the repulsive In–In interactions in In_3Pd_2 and InPd NPs.

$InPd_3$ NPs exhibit sharp In–In peaks within the stability domain $\mathscr{S}$, at $r \simeq 3.0$ Å and $r \simeq 4.0$ Å for both chemically ordered and disordered structures. After relaxation, peaks remain sharp notably for chemically disordered NPs. Such NPs are crystalline (Fig. 6, right), the crystalline character resulting from the attractive In–In interactions Fig. 6, right, plotted in brown). Both InPd and In_3Pd_2 NPs show similar behaviours, distinct from the one observed for $InPd_3$, with sharp and large In–In RDF peaks in the $\mathscr{S}$ region for chemically ordered and disordered NPs, respectively. Upon relaxation, the RDF plots do not change much for ordered NPs, and at most

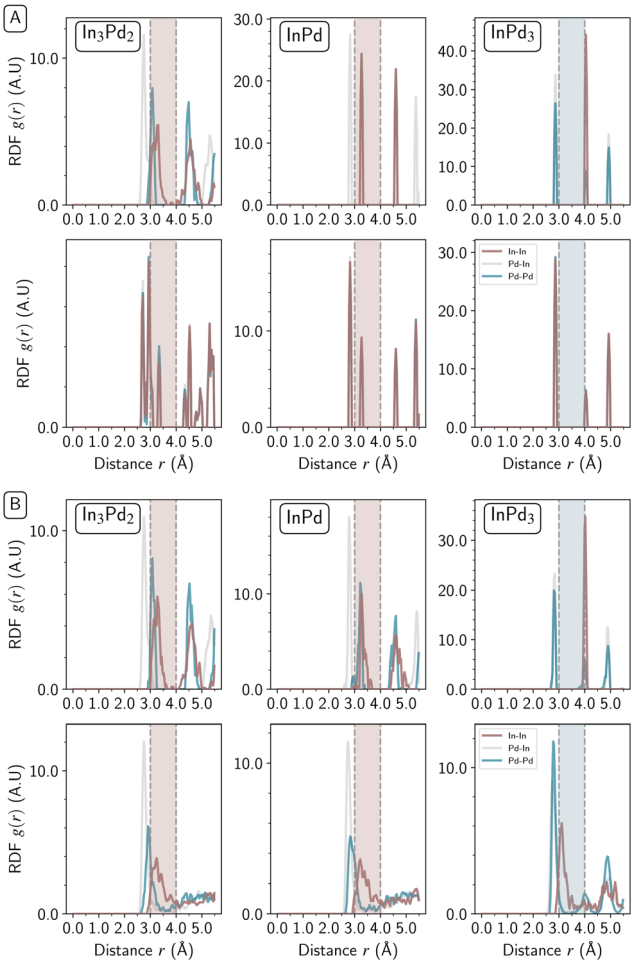

Fig. 9 Radial distribution function of In–In (brown), Pd–Pd (blue) and In–Pd (grey) bonds for small Pd-rich Wulff polyhedra nanoparticles (diameter 24 Å) of In_3Pd_2 (left), InPd (middle), and $InPd_3$ (right) compounds. The top row displays ordered WP_{Pd}, whereas the bottom row represents disordered WP_{Pd}. Radial function distributions for non-relaxed and relaxed nanoparticles are shown in Fig. 9A (top) and B (bottom), respectively. Blue filled area represents the attractive domain of In–In interactions in $InPd_3$ NPs. Red filled areas represent the repulsive domain of In–In interactions in In_3Pd_2 and InPd NPs. ($\mathscr{S}$ = [3.0 Å, 4.0 Å]).

there is a slight broadening of peaks for In–Pd NPs, while the RDF features are strongly modified in the case of disordered NPs. Based on the previous pair interaction analysis (Fig. 8), short In–In bonds (<3 Å) are highly repulsive, *i.e.* much more repulsive than in the $\mathscr{S}$ region. Thus, bond lengths should increase to reduce energetically destabilising In–In interactions. Indeed, after relaxation, In–In RDF peaks disappeared at $r < 3$ Å, and the shortest In–In peak here lay at $r = 3.3$ Å. Hence, the combination of chemical disorder and In–In bond length increase is demonstrated to drive the tendency towards amorphisation of chemically disordered InPd and In_3Pd_2 NPs. To summarise, In–In interactions destabilise the chemically disordered In_3Pd_2 and InPd NPs, leading to amorphisation. In contrast, the favourable In–In interactions observed for $InPd_3$ nanoparticles contribute to their stabilisation, and support their crystalline character.

2.5 NP work functions, impact of the surface composition and structure

The work function (WF), *i.e.* the energy barrier of an electron escaping from the surface, is a fundamental material property, with many applications, especially, those involving electron exchanges at the material's surface, such as adsorption. Thus, it is directly linked to catalytic properties, as illustrated in the literature.[82,83] Although it lacks direct structural and chemical information, it can be a powerful tool to design optimised catalyst materials.[57,84–90]

The first successful calculations of WFs for simple metal surfaces have been achieved on the basis of a jellium model and a slab method by Lang and Kohn[91]:

$$W_{\text{slab}} = \lim_{\|\boldsymbol{r}\|\to+\infty} \langle V_{\text{LP}} \rangle_{(\boldsymbol{r},\boldsymbol{n})} - \varepsilon_{\text{F}}, \tag{3}$$

where $\boldsymbol{r} \in \mathbb{R}^{3N}$ shows the system coordinates, ε_{F} is the Fermi level, V_{LP} is the potential energy and $\langle V_{\text{LP}} \rangle_{(\boldsymbol{r},\boldsymbol{n})}$ is its averaged value in a plane defined by $\boldsymbol{n}$ (normal surface vector). The computation of $\langle V_{\text{LP}} \rangle_{(\boldsymbol{r},\boldsymbol{n})}$ is rather easy using slabs, but can be influenced by quantum-size effects, as discussed in the literature.[92–94] Nevertheless, over the years, WFs have been computed for a wide range of materials, using this approach.[95–99]

In the case of NPs, the previous pseudo one-dimension scheme cannot be used. Thus, we propose to introduce a new methodology to compute NP WFs, based on the Lang and Kohn's work[91]:

$$W_{\text{NP}}(\delta r) = \lim_{\|\boldsymbol{r}\|\to+\infty} \langle V_{\text{LP}} \rangle(r, \delta r) - \varepsilon_{\text{F}}, \tag{4}$$

where $\langle V_{\text{LP}} \rangle$ $(r,\delta r)$ is the radial averaged potential energy function (see eqn (S9), ESI†). We successfully validated our method by comparing computational results with experimental data obtained from gold nanoparticles (Fig. 10 and Table S4, Fig. S1 for more details about the procedure, ESI†).[100] Sizes of

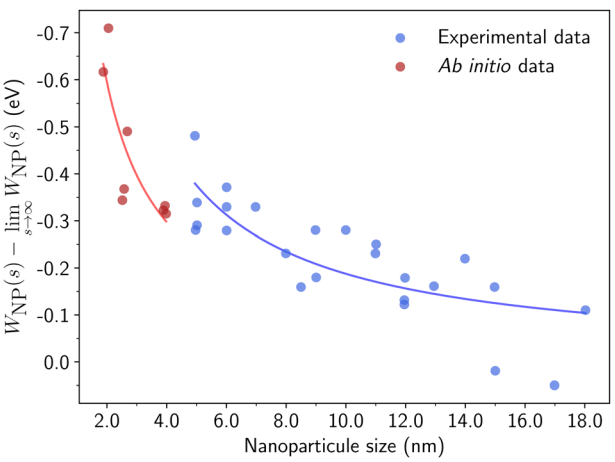

Fig. 10 Direct comparison between computed and measured work functions for gold NPs. Experimental data (in blue) are extracted from ref. 100 and *ab initio* work functions (in red) are calculated based on our methodology.

calculated nanoparticles have been evaluated by examining the variations in $\langle V_{LP} \rangle$ as a function of the distance from their centre. Relative work functions have been considered, *i.e.* $\Delta W = W_{NP} - W_{NP}^{\infty}$, where W_{NP}^{∞} is the limit of the NP work function when its size tends towards infinity. This approach is adopted because the experimental measurements are conducted on supported nanoparticles, while the calculations are performed on isolated nanoparticles. The comparison of relative values serves to correct for substrate influence and potential measurement-related shifts, providing a means to align the experimental and calculated results. Although the size domains explored in the calculations (2–4 nm) and in the experimental approach (larger than 4 nm) slightly differ, the variations of the work functions with the NP sizes exhibit strong consistencies. Moreover, the trends nicely align a coulombic decay with the nanoparticle size, as expected by a simple electrostatic model.[101] This strengthens the overall confidence in the reliability and applicability of our computational methodology.

The WFs computed for crystalline and amorphous In–Pd NPs are presented in Fig. 11 (values in Table S4, and DOS in Fig. S2, ESI†). They are found to be of the same order of magnitude as infinite slabs, and rather different from the ones of pure In and pure Pd surfaces, thus highlighting an alloy effect, as frequently reported in the literature (for instance, see ref. 102,103). Our results suggest tiny size effects, since the work functions of larger NPs are larger than those of smaller particles with similar surface compositions. According to the jellium model, the difference in work functions is expected to be of the order of 0.07 eV.[101,104] But we observed a smaller difference (0.03 eV) between the WFs of the 369 and 1105 atoms-InPd WP_{Pd} NPs with similar surface Pd contents (0.48 and 0.49 at%, respectively). The chemical potential drastically impacts NP WFs: for instance, the WFs of the small In_3Pd_2 WP_{Pd} and WP_{In} differ by roughly 0.15 eV, and reaches approximately 0.5 eV for InPd NPs. Moreover, the correlation of the WFs with the Pd surface content is clearly observed (Fig. 11), the correlation being roughly linear.

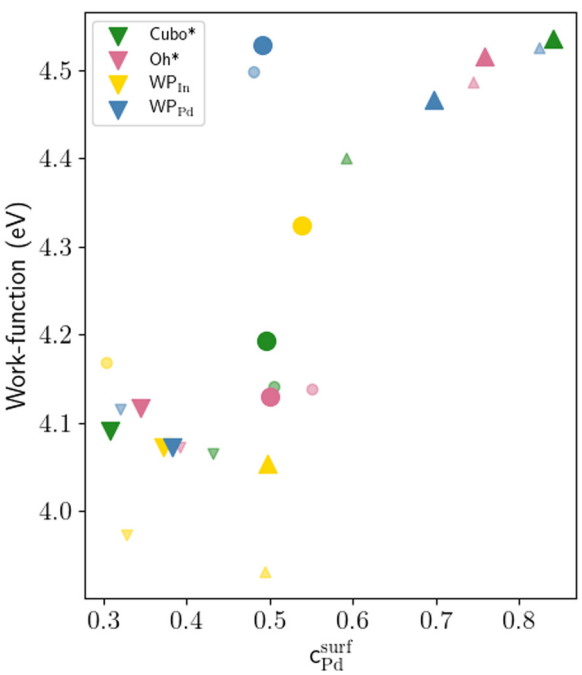

Fig. 11 Work function (in eV) as a function of the surface Pd concentration (in at%). Small and large symbols correspond to small and large nanoparticles, respectively. Colours give the NP morphologies, while symbols give the compounds (∇In_3Pd_2, ○InPd, and ΔInPd$_3$) from which they have been built. Data are gathered in Table S4 (ESI†).

Finally, we quantitatively compare the WF difference between small ordered NPs described in Fig. 6 (top row) and small chemically disordered NPs, with same size and composition, generated randomly. Work functions of disordered NPs are gathered in Table 2, along with $\langle \Delta W_{NP} \rangle$, a parameter introduced to quantify the changes in WFs induced by disorder/amorphisation and defined by:

$$\langle \Delta W_{NP} \rangle (N^{dis}) = \frac{1}{N^{dis}} \sum_{i=1}^{N^{dis}} \left(W_{NP}^{ord} - W_{NP}^{dis}(i) \right), \qquad (5)$$

where N^{dis} is the number of configurations considered to describe one disordered nanoparticle, while W_{NP}^{ord} and $W_{NP}^{dis}(i)$ are the work functions of ordered and disordered NPs (labelled with i), respectively. The standard error $\sigma(W_{NP}^{dis})/\sqrt{N^{dis}}$ of $\langle \Delta W_{NP} \rangle$ is calculated based on its standard deviation $\sigma(W_{NP}^{dis})$. In all cases, the computed standard error is small in comparison to $\langle \Delta W_{NP} \rangle$, which means that values of $\langle \Delta W_{NP} \rangle$ are statistically significant.

On the one hand, the change in WFs ($\langle \Delta W_{NP} \rangle$) for $InPd_3$ WP_{Pd} NPs is tiny and slightly negative with a rather large – larger than in the other cases – standard error value. This is consistent with the previous structural analysis. Only small structural differences have been observed between ordered and disordered NPs in this case, the crystalline character of the $InPd_3$ WP_{Pd} NP being kept when disorder is introduced. Thus, the WF modification ($\langle \Delta W_{NP} \rangle$) only comes from a surface Pd content that may slightly differ from the one in the ordered NP.

On the other hand, the change in WFs ($\langle \Delta W_{NP} \rangle$) for InPd and In_3Pd_2 WP_{Pd} NPs is positive and rather large, of the order of 0.2 eV. This result is quite different from the one for $InPd_3$ WP_{Pd} NPs, and may be induced by the structural changes investigated above, especially, the tendency towards amorphisation observed for disordered WP_{Pd} InPd and In_3Pd_2 NPs. Here, the change in WFs mainly comes from the modification of the NP surface structure.

Table 2 WF differences between (chemically) ordered and disordered NPs, along with the standard error deviation

NP	N^{dis}	$\langle \Delta W_{NP} \rangle$ (N^{dis}) (eV)	$\sigma(W_{NP}^{dis})/\sqrt{N^{dis}}$ (eV)
In_3Pd_2 WP_{Pd}	9	0.1842	0.005
InPd WP_{Pd}	9	0.246	0.007
$InPd_3$ WP_{Pd}	10	−0.0431	0.010

3 Conclusions

This study contributes to a better understanding of structure-properties in NPs, through the investigation of In–Pd NPs built from bulk In_3Pd_2, InPd and $InPd_3$ intermetallics. According to surface energies, ordered NPs likely present crystalline forms, the Wulff polyhedron being the most stable NP shape in the range of 300–1200 atoms. A noticeable tendency towards amorphisation is observed when disorder is introduced in NPs built from In_3Pd_2 and InPd, driven by non-favourable In–In interactions. Tuning the NP surface structure and composition modifies the NP work function, with variations of the order of 0.5 eV. Non-crystalline morphologies, such as Ih or Dh, are not likely. This original behaviour compared to that observed in metals and TM–TM alloys, likely stems from the rather elevated formation enthalpy of pM–TM intermetallics.

The current study is limited to three In–Pd phases with rather small crystal cells, and already gives important insights. More complex phases do exist in the phase diagram of In–Pd, thus challenging the interplay between bulk structures and 3-dimensional NP morphologies built from them. Indeed, in addition to the selection of the termination plane discussed in the present paper, several questions arise when considering more complex compounds. Actually, the approach based on the Wulff construction should be adapted in the case of facets whose structure is only a fraction of the periodic surface. More generally, when the crystal cell is much larger than the NP size, one may expect that the different parts of the crystal are not equivalent towards nanoparticle formation, as, for instance, the clusters generally used to represent the structure of such complex intermetallics.[105] Finally, because most heterogeneous reactions catalysed by nanoparticles occur at relatively high temperatures, molecular dynamic simulations could be useful to identify dynamical modulations of NP morphologies during reactions.[106]

4 Computational details

Electronic structure spin polarised calculations have been performed for static NPs with the plane wave Vienna ab initio simulation package (VASP),[78–80] using the projector augmented wave (PAW) method,[107,108] the generalised gradient approximation (GGA-PBE),[109,110] and an energy cutoff set to 450 eV. Ten valence electrons have been explicitly treated for Pd ($5s^1\ 4d^9$) and three for In ($5s^2\ 5p^1$).

Total energies have been minimised until the energy differences became less than 10^{-5} eV between two electronic cycles. Atomic structures have been relaxed till the Hellmann–Feynman forces are as low as 0.01 eV $Å^{-1}$. Structures were plotted using the OVITO software.[111]

For each composition, bulk-, slab- and nanoparticle-type calculations have been performed. The different systems have been built with ASE[112] combined to MPInterfaces[113] and pymatgen.[114] The Brillouin zones of the different systems have been sampled with Γ-centred Monkhorst–Pack k-point meshes. Infinite surfaces have been modelled with symmetric slabs (Table S1, ESI†), separated by a void thickness larger than 20 Å. Nanoparticles have been computed in large cubic simulation boxes (parameter equal to 50 Å). Only one k-point has been used for the calculations with nanoparticles. The stabilities of the considered systems have been computed using formation enthalpies for bulk and NP stems (Table 1 and Table S5, ESI†) and surface energies as a function of the Pd's chemical potential for slabs (see the ESI,† Section S2).[115] For NPs, historically, stabilities are evaluated through the Δ descriptor:

$$\Delta = \frac{E_{\text{tot}}^{\text{NP}} - \sum_{i=1}^{M} N_i E_i^{\text{coh}}}{\left(\sum_{i=1}^{M} N_i\right)^{2/3}} \tag{6}$$

where $E_{\text{tot}}^{\text{NP}}$ is the total energy of the NP composed of M elements, E_i^{coh} is the bulk cohesive energy of the i species and N_i is the number of atom i in the nanoparticle. The Δ descriptor approximates the number of surface atoms by $\left(\sum_{i=1}^{M} N_i\right)^{2/3}$, which is not accurate for small NPs. In this work, stabilities of NPs are evaluated through surface energies (γ_{NP}):

$$\gamma_{\text{NP}} = \frac{1}{A_{\text{NP}}}(E_{\text{tot}}^{\text{NP}} - n_{\text{Pd}}\mu_{\text{Pd}} - n_{\text{In}}\mu_{\text{In}}) \tag{7}$$

where A_{NP} is the NP surface area, computed with Ovito[111] based on the Gaussian density method.[116] The quantities μ_{Pd} and μ_{In} (respectively, n_{Pd} and n_{In}) are the chemical potentials (respectively, number of atoms) of Pd and In in the nanoparticle. The chemical potentials of Pd and In are not independent, since:

$$(x + y)\Delta H_{\text{f}}(\text{In}_x\text{Pd}_y) = x(\mu_{\text{Pd}} - \mu_{\text{Pd}}{}^{\text{b}}) + y(\mu_{\text{In}} - \mu_{\text{In}}{}^{\text{b}}) \tag{8}$$

Assuming an equilibrium between the surface and the underlying NP core (assimilated to bulk), the chemical potentials are confined in a given range, *i.e.*

$$\frac{(x + y)\Delta H_{\text{f}}}{y} \leq \Delta\mu_{\text{Pd}} \leq 0 \tag{9}$$

where $\Delta\mu_{\text{Pd}} = \mu_{\text{Pd}} - \mu_{\text{Pd}}{}^{\text{b}}$.

Conflicts of interest

There are no conflicts to declare.

Acknowledgements

This work was granted access to the high performance computing (HPC) resources of IDRIS and TGCC under the allocation 99642 attributed by GENCI. HPC resources were also partially provided by the EXPLOR centre hosted by the Université de Lorraine (project 2017M4XXX0108). One of us thanks Dr David Loffreda for fruitful discussions. This work is supported by the European Integrated Centre for the Development of New Metallic Alloys and Compounds. Some of us acknowledge financial support through the COMETE project (COnception

in silico de Matériaux pour l'EnvironnemenT et l'énergie) cofunded by the European Union under the program FEDER-FSE Lorraine et Massif des Vosges 2014-2020. One of us thanks financial support from ''Lorraine Université d'Excellence''.

References

1 I. Freestone, N. Meeks, M. Sax and C. Higgitt, *Gold Bull.*, 2007, **40**, 270.
2 J. Jeevanandam, A. Barhoum, Y. Chan, A. Dufresne and M. Danquah, *Beilstein J. Nanotechnol.*, 2018, **9**, 1050.
3 *Fundamentals and Applications of Nano Silicon in Plasmonics and Fullerines*, ed. M. Nayfeh, Elsevier, 2018, pp. 497–518.
4 E. C. Dreaden, A. M. Alkilany, X. Huang, C. J. Murphy and M. A. El-Sayed, *Chem. Soc. Rev.*, 2012, **41**, 2740.
5 C. Shasha and K. Krishnan, *Adv. Mater.*, 2021, **33**, 1904131.
6 S. Campora and G. Ghersi, *Nanotechnol. Rev.*, 2022, **11**, 2595.
7 H. You, S. Yang, B. Ding and H. Yang, *Chem. Soc. Rev.*, 2013, **42**, 2880.
8 D. J. de Aberasturi, A. B. Serrano-Montes and L. M. Liz-Marzan, *Adv. Opt. Mater.*, 2015, **3**, 602.
9 A. Kumar, P. Choudhary, A. Kumar, P. H. C. Camargo and V. Krishn, *Small*, 2022, **18**, 2101638.
10 J. A. Darr, J. Zhang, N. M. Makwana and X. Weng, *Chem. Rev.*, 2017, **117**, 11125.
11 L. Wang, M. H. Kafshgari and M. Meunier, *Adv. Funct. Mater.*, 2020, **30**, 2005400.
12 J. Grunes, J. Zhu and G. Somorjai, *Chem. Commun.*, 2003, 2257.
13 T. Bligaard and J. Norskov, in *Chemical Bonding at Surfaces and Interfaces*, ed. A. Nilsson, L. G. Pettersson and J. K. Norskov, Elsevier, 2008, Chapter 4 – Heterogeneous Catalysis, p. 255.
14 J. R. Ludwig and C. S. Schindler, *Chem*, 2017, **2**, 313.
15 D. Wang and D. Astruc, *Chem. Soc. Rev.*, 2017, **46**, 816.
16 M. Haruta, T. Kobayashi, H. Sano and N. Yamada, *Chem. Lett.*, 1987, 405.
17 S. Vukojevic, O. Trapp, J.-D. Grunwaldt, C. Kiener and F. Schüth, *Angew. Chem.*, 2005, **117**, 8192.
18 X. Liu, J. Iocozzia, Y. Wang, X. Cui, Y. Chen, S. Zhao and Z. Li, *Energy Environ. Sci.*, 2017, **10**, 402.
19 Z. W. Seh, J. Kibsgaard, C. F. Dickens, I. Chorkendorff, J. K. Norskov and T. F. Jaramillo, *Science*, 2017, **355**, eaad4998.
20 L. Liu and A. Corma, *Chem. Rev.*, 2018, **118**, 4981.
21 A. Medford, A. Vojvodic, J. S. Hummelshoj, J. Voss, F. Abild-Pedersen, F. Studt, T. Bligaard, A. Nilsson and J. K. Norskov, *J. Catal.*, 2015, **328**, 36.
22 J. Norskov, F. Studt, F. Abild-Pedersen and T. Bligaard, *Fundamental Concepts in Heterogeneous Catalysis*, John Wiley & Sons Inc., 2014.
23 A. Vojvodic and J. K. Nørskov, *Natl. Sci. Rev.*, 2015, **2**, 140.
24 M. Armbruester, *Sci. Technol. Adv. Mater.*, 2020, **21**, 303.
25 Y. Nakaya and S. Furukawa, *Chem. Rev.*, 2023, **123**, 5859.
26 B. G. Pollet, S. S. Kocha and I. Staffell, *Curr. Opin. Electrochem.*, 2019, **16**, 90.
27 V. Stamenkovic, T. Schmidt, P. Ross and N. Markovic, *J. Electroanal. Chem.*, 2003, **554**, 191.
28 V. R. Stamenkovic, B. Fowler, B. S. Mun, G. Wang, P. N. Ross, C. A. Lucas and N. M. Markovic, *Science*, 2007, **315**, 493.
29 R. Ferrando, J. Jellinek and R. L. Johnston, *Chem. Rev.*, 2008, **108**, 845.
30 A. Jain, S. P. O. G. Hautier, W. Chen, W. D. Richards, W. Dacek, S. Cholia, D. Gunter, D. Skinner, G. Ceder and K. A. Persson, *APL Mater.*, 2013, **1**, 011002.
31 J. E. Montoya-Cardona, A. Salichon, N. Tarrat, E. Gaudry and D. Loffreda, *J. Phys. Chem. C*, 2023, **127**, 18043.
32 N. Köwitsch, L. Thoni, B. Klemmed, A. Benad, P. Paciok, M. Heggen, I. Köwitsch, M. Mehring, A. Eychmüller and M. Armbrüster, *ACS Catal.*, 2021, **11**, 304–312.
33 A. Garcia-Trenco, A. Regoutz, E. R. White, D. J. Payne, M. S. Shaffer and C. K. Williams, *Appl. Catal., B*, 2018, **220**, 9.
34 P. Wu and B. Yang, *Catal. Sci. Technol.*, 2019, **9**, 6102.
35 Z. Wu, E. Wegener, H.-T. Tseng, J. R. Gallagher, J. W. Harris, R. E. Diaz, Y. Ren, F. H. Ribeiro and J. T. Miller, *Catal. Sci. Technol.*, 2016, **6**, 6965.
36 Y. Luo, S. Alarcón Villaseca, M. Friedrich, D. Teschner, A. Knop-Gericke and M. Armbrüster, *J. Catal.*, 2016, **338**, 265–272.
37 Y. Cao, Z. Sui, Y. Zhu, X. Zhou and D. Chen, *ACS Catal.*, 2017, **7**, 7835–7846.
38 P. Markov, A. Bukhtiyarov, I. Mashkovsky, N. S. Smirnova, I. P. Prosvirin, Z. S. Vinokurov, M. A. Panafidin, G. N. Baeva, Y. V. Zubavichus, V. I. Bukhtiyarov and A. Y. Stakheev, *Kinet. Catal.*, 2019, **60**, 842.
39 S. Chen, X. Huang, D. Schild, D. Wang, C. Kübel and S. Behrens, *Nanoscale*, 2022, **14**, 17661.
40 D. Pavesi, F. S. M. Ali, D. Anastasiadou, T. K. M. Figueiredo, G.-J. M. Gruter, M. T. M. Koper and K. J. P. Schouten, *Catal. Sci. Technol.*, 2020, **10**, 4264.
41 Q. Feng, S. Zhao, Y. Wang, J. Dong, W. Chen, D. He, D. Wang, J. Yang, Y. Zhu, H. Zhu, L. Gu, Z. Li, Y. Liu, R. Yu, J. Li and Y. Li, *J. Am. Chem. Soc.*, 2017, **139**, 7294–7301.
42 C. Wolverton and V. Ozolins, *Phys. Rev. B: Condens. Matter Mater. Phys.*, 2006, **73**, 144104.
43 R. Ferro and A. Saccone, *Intermetallic Chemistry*, Pergamon Elsevier, Oxford, UK, 2008.
44 C. White and H. Okamoto, *Phase Diagrams of Indium Alloys and their Engineering Applications*, 1992.
45 M. Neumann, D. Teschner, A. Knop-Gericke, W. Reschetilowski and M. Armbruester, *J. Catal.*, 2016, **340**, 49.
46 J. Pirart, A. Front, D. Rapetti, C. Andreazza-Vignolle, P. Andreazza, C. Mottet and R. Ferrando, *Nat. Commun.*, 2019, **10**, 1982.
47 F. Tournus, K. Sato, T. Epicier, T. J. Konno and V. Dupuis, *Phys. Rev. Lett.*, 2013, **110**, 055501.
48 J. Penuelas, P. Andreazza, C. Andreazza-Vignolle, H. C. N. Tolentino, M. De Santis and C. Mottet, *Phys. Rev. Lett.*, 2008, **100**, 115502.

49 M. Zhou, C. Li and J. Fang, *Chem. Rev.*, 2021, **121**, 736.
50 P. Makkar and N. N. Ghosh, *RSC Adv.*, 2021, **11**, 27897.
51 H. Demir and L. C. Grabow, *ACS Appl. Nano Mater.*, 2020, **3**, 6127.
52 D. Vollath, F. Fischer and D. Holec, *Beilstein J. Nanotechnol.*, 2018, **9**, 2265.
53 H. Amara, J. Nelayah, J. Creuze, A. Chmielewski, D. Alloyeau, C. Ricolleau and B. Legrand, *Phys. Rev. B*, 2022, **105**, 165403.
54 A. Chmielewski, J. Nelayah, H. Amara, J. Creuze, D. Alloyeau, G. Wang and C. Ricolleau, *Phys. Rev. Lett.*, 2018, **120**, 025901.
55 L. Lin, R. Jacobs, T. Ma, D. Chen, J. Booske and D. Morgan, *Phys. Rev. Appl.*, 2023, **19**, 037001.
56 F. Calle-Vallejo, M. T. M. Koper and A. S. Bandarenka, *Chem. Soc. Rev.*, 2013, **42**, 5210.
57 S. Trasatti, *J. Electroanal. Chem.*, 1972, **39**, 163.
58 H. Kohlmann, *J. Solid State Chem.*, 2010, **183**, 367.
59 I. Harris, M. Norman and A. W. Bryant, *J. Less-Common Met.*, 1968, **16**, 427.
60 C. Garnero, M. Lepesant, C. Garcia-Marcelot, Y. Shin, C. Meny, P. Farger, B. Warot-Fonrose, R. Arenal, G. Viau, K. Soulantica, P. Fau, P. Poveda, L.-M. Lacroix and B. Chaudret, *Nano Lett.*, 2019, **19**, 1379–1386.
61 A. Front and C. Mottet, *J. Phys. Chem. C*, 2021, **125**, 16358–16365.
62 Y. Yang, C.-C. Chen, M. C. Scott, C. Ophus, R. Xu, A. Pryor, L. Wu, F. Sun, W. Theis, J. Zhou, M. Eisenbach, P. R. C. Kent, R. F. Sabirianov, H. Zeng, P. Ercius and J. Miao, *Nature*, 2017, **542**, 75–79.
63 S. Amore, S. Delsante, N. Parodi and G. Borzone, *Thermochim. Acta*, 2009, **481**, 1.
64 A. Ciccioli, G. Balducci, G. Gigli, L. Perring and F. Bussy, *Intermetallics*, 2000, **8**, 195.
65 A. Ormeci, E. Gaudry, M. Armbrüster and Y. Grin, *ChemistryOpen*, 2022, 11.
66 N. Roy, A. Chakrabarty, B. Koley, T. Saha-Dasgupta and P. P. Jana, *J. Solid State Chem.*, 2020, **290**, 121567.
67 G. Wulff, *Z. Kristallogr. - Cryst. Mater.*, 1901, **34**, 449–530.
68 H. Wang, S. Zhou, K. D. Gilroy, Z. Cai and Y. Xia, *Nano Today*, 2017, **15**, 121–144.
69 G. Casillas, J. J. Velazquez-Salazar and M. Jose-Yacaman, *J. Phys. Chem. C*, 2012, **116**, 8844.
70 A. Front and C. Mottet, *J. Phys. Chem. C*, 2021, **125**, 16358–16365.
71 A. Front and C. Mottet, *Theor. Chem. Acc.*, 2022, **141**, 2.
72 K. Loza, M. Heggen and M. Epple, *Adv. Funct. Mater.*, 2020, **30**, 1909260.
73 B. Farkas and N. H. de Leeuw, *Nanotechnology*, 2020, **31**, 195711.
74 H. Yang, K. Wang, Z. Tang, Z. Liu and S. Chen, *J. Catal.*, 2020, **382**, 181–191.
75 D. Alloyeau, C. Ricolleau, C. Mottet, T. Oikawa, C. Langlois, Y. Le Bouar, N. Braidy and A. Loiseau, *Nat. Mater.*, 2009, **8**, 940.
76 R. Dronskowski and P. E. Bloechl, *J. Phys. Chem.*, 1993, **97**, 8617–8624.
77 S. Maintz, V. L. Deringer, A. L. Tchougréeff and R. Dronskowski, *J. Comput. Chem.*, 2016, **37**, 1030–1035.
78 G. Kresse and J. Hafner, *Phys. Rev. B: Condens. Matter Mater. Phys.*, 1993, **47**, 558–561.
79 G. Kresse and J. Furthmüller, *Comput. Mater. Sci.*, 1996, **6**, 15–50.
80 G. Kresse and J. Furthmüller, *Phys. Rev. B: Condens. Matter Mater. Phys.*, 1996, **54**, 11169–11186.
81 L. Pauling, *The Nature of the Chemical Bondâ€"An Introduction to Modern Structural Chemistry*, Cornell University Press, New-York, 1960.
82 T. Liu, C. Xi, C. Dong, C. Cheng, J. Qin, S. Hu, H. Liu and X.-W. Du, *J. Phys. Chem. C*, 2019, **123**, 28319–28326.
83 A. M. Ismail, E. Csapó and C. Janáky, *Electrochim. Acta*, 2019, **313**, 171–178.
84 X. Luo, R. Jiang, Z. Ma, T. Yang, H. Liu, W. Wu, C. Dong and X.-W. Du, *Phys. Chem. Chem. Phys.*, 2022, **24**, 9188.
85 C. Vayenas, S. Bebelis and S. Ladas, *Nature*, 1990, **343**, 625.
86 B. Caglar, A. C. Kizilkaya, J. W. Niemantsverdriet and C. J. Weststrate, *Catal., Struct. React.*, 2018, **4**, 1.
87 C. Beasley, M. K. Gnanamani, E. Santillan-Jimenez, M. Martinelli, W. D. Shafer, S. D. Hopps, N. Wanninayake and D.-Y. Kim, *ChemistrySelect*, 2020, **5**, 1013.
88 X. Wang, G. Zhang, L. Yang, E. Sharman and J. Jiang, *WIREs Comput. Mol. Sci.*, 2018, **8**, e1369.
89 A. Zeradjanin, A. Vimalanandan, G. Polymeros, A. A. Topalov, K. J. J. Mayrhofer and M. Rohwerder, *Phys. Chem. Chem. Phys.*, 2017, **19**, 17019.
90 Y. Zhou, G. Zhang, Q. Ji, W. Zhang, J. Zhang and H. Liu, *Environ. Sci. Technol.*, 2019, **53**, 11383.
91 N. D. Lang and W. Kohn, *Phys. Rev. B: Solid State*, 1971, **3**, 1215–1223.
92 N. E. Singh-Miller and N. Marzari, *Phys. Rev. B: Condens. Matter Mater. Phys.*, 2009, **80**, 235407.
93 S. De Waele, K. Lejaeghere, M. Sluydts and S. Cottenier, *Phys. Rev. B*, 2016, **94**, 235418.
94 J. C. Boettger, *Phys. Rev. B: Condens. Matter Mater. Phys.*, 1996, **53**, 13133.
95 J. Wang and S.-Q. Wang, *Surf. Sci.*, 2014, **630**, 216–224.
96 D.-P. Ji, Q. Zhu and S.-Q. Wang, *Surf. Sci.*, 2016, **651**, 137–146.
97 S.-H. Yoo, N. Siemer, M. Todorova, D. Marx and J. Neugebauer, *J. Phys. Chem. C*, 2019, **123**, 5495–5506.
98 R. Tran, X.-G. Li, J. H. Montoya, D. Winston, K. A. Persson and S. P. Ong, *Surf. Sci.*, 2019, **687**, 48–55.
99 T. T. Dorini, F. Brix, C. Chatelier, A. Kokalj and E. Gaudry, *Nanoscale*, 2021, **13**, 10771–10779.
100 Y. Zhang, O. Pluchery, L. Caillard, A.-F. Lamic-Humblot, S. Casale, Y. J. Chabal and M. Salmeron, *Nano Lett.*, 2015, **15**, 51.
101 E. Kalered, N. Brenning, I. Pilch, L. Caillault, T. Minea and L. Ojamae, *Phys. Plasmas*, 2017, 24.
102 S. C. Fain and J. M. McDavid, *Phys. Rev. B: Solid State*, 1974, **9**, 5099.
103 P. D. Swartzentruber, M. J. Detisch and T. J. Balk, *J. Vac. Sci. Technol.*, 2015, **33**, 021405.

104 K. F. Wojciechowski, *Phys. Rev. B: Condens. Matter Mater. Phys.*, 1999, **60**, 9202.
105 T. G. Akhmetshina, V. A. Blatov, D. M. Proserpio and A. P. Shevchenko, *Acc. Chem. Res.*, 2018, **51**, 21.
106 X. Liu, X. Wen and R. Hoffmann, *ACS Catal.*, 2018, **8**, 3365.
107 P. E. Blöchl, *Phys. Rev. B: Condens. Matter Mater. Phys.*, 1994, **50**, 17953–17979.
108 G. Kresse and D. Joubert, *Phys. Rev. B: Condens. Matter Mater. Phys.*, 1999, **59**, 1758–1775.
109 J. P. Perdew, K. Burke and M. Ernzerhof, *Phys. Rev. Lett.*, 1996, **77**, 3865.
110 J. P. Perdew, K. Burke and M. Ernzerhof, *Phys. Rev. Lett.*, 1997, **78**, 1396.
111 A. Stukowski, *Modell. Simul. Mater. Sci. Eng.*, 2009, **18**, 015012.
112 A. H. Larsen, J. J. Mortensen, J. Blomqvist, I. E. Castelli, R. Christensen, M. Dulak, J. Friis, M. N. Groves, B. Hammer, C. Hargus, E. D. Hermes, P. C. Jennings, P. B. Jensen, J. Kermode, J. R. Kitchin, E. L. Kolsbjerg, J. Kubal, K. Kaasbjerg, S. Lysgaard, J. B. Maronsson, T. Maxson, T. Olsen, L. Pastewka, A. Peterson, C. Rostgaard, J. Schiøtz, O. Schütt, M. Strange, K. S. Thygesen, T. Vegge, L. Vilhelmsen, M. Walter, Z. Zeng and K. W. Jacobsen, *J. Phys.: Condens.Matter*, 2017, **29**, 273002.
113 K. Mathew, A. K. Singh, J. J. Gabriel, K. Choudhary, S. B. Sinnott, A. V. Davydov, F. Tavazza and R. G. Hennig, *Comput. Mater. Sci.*, 2016, **122**, 183–190.
114 S. P. Ong, W. D. Richards, A. Jain, G. Hautier, M. Kocher, S. Cholia, D. Gunter, V. L. Chevrier, K. A. Persson and G. Ceder, *Comput. Mater. Sci.*, 2013, **68**, 314–319.
115 Émilie Gaudry, in *Comprehensive Inorganic Chemistry III*, ed. J. Reedijk and K. R. Poeppelmeier, Elsevier, Oxford, 3rd edn, 2023, pp. 74–104.
116 M. Krone, J. Stone, T. Ertl and K. Schulten, EuroVis - Short Papers, 2012.